9th ECCOMAS Thematic Conference on the Mechanical Response of Composites
COMPOSITES 2023
G. Catalanotti, H. Petterman and G. Pittaresi (Eds)

EFFECT OF PLY THICKNESS ON DYNAMIC DAMAGE PROGRESSION IN CROSS-PLY LAMINATES UNDER LOW-VELOCITY IMPACT

Onur Ali Batmaz[1,2], Demirkan Coker[1,2*]

[1] Department of Aerospace Engineering, Middle East Technical University (METU), Ankara, Turkey
[2] METU Center for Wind Energy Research (RÜZGEM), METU, Ankara, Turkey
*coker@metu.edu.tr

Keywords: Low-velocity impact, Cross-ply CFRP laminates, Damage mechanics

Summary: *In this study, we have conducted in-situ LVI experiments on cross-ply CFRP beams having stacking layups $[0_4/90_4/0_2]s$ and $[0_2/90_2/0_2/90_2/0_2]s$. The progression of damage is observed through high-speed photography. In addition to LVI, quasi-static indentation (QSI) experiments are performed to reduce challenges in monitoring damage progression during the short impact loading interval. QSI experiments provide magnified in-situ observations on the free edge of the beam using a traveling digital microscope. Numerical simulations of these experiments are carried out using the finite element method in ABAQUS/Explicit. The orthotropic constitutive material model, predicting fiber and matrix damage initiation and evolution, is implemented through a VUMAT subroutine. The comparison between numerical simulations and experimental observations allowed us to investigate the influence of ply clustering on the LVI-induced damage mechanisms.*

1 INTRODUCTION

Impact events have the potential to induce internal failures, such as matrix cracking and delamination, leading to substantial reductions in the structural strength and stiffness [1]. The significance of impact-induced damage becomes especially critical when it occurs on the outer surfaces and remains barely visible or entirely undetectable. This often happens as a consequence of low-energy, low-velocity impact (LVI) incidents.

Identifying damage mechanisms in composite laminates under LVI loadings can be complicated when considering layup configurations designed for practical engineering applications. In such configurations, primary damage mechanisms might be obscured, and the layup design itself might introduce other modes of damage. Conversely, layup choices like cross-ply configurations often exhibit only transverse matrix cracking initially, making them a preferred choice for investigating damage mechanisms due to their simplified behavior. In the context of damage mechanisms within cross-ply configurations, Parvizzi [2] and Flaggs and Kural [3] have reported that the strengths of carbon and glass fiber-reinforced plastic (FRP) cross-ply laminates are influenced by the number of embedded 90° plies. This observation has been attributed to the constraining effect of the 0° plies on the properties of 90° plies. Further investigations have indicated that the actual strength of a laminate depends not only on the properties of its constituent lamina, but also on the layup configuration, encompassing the positioning of angled plies, the alignment of adjacent layers, and the thickness of the plies [2,4]. In the literature, this actual strength is referred to as the “in-situ strength”.

The observed connection between the actual strength and the number of embedded plies has driven investigations into the impacts of ply clustering on laminated composites. Wisnom et al. demonstrated that stacking more plies with matching fiber orientations within a quasi-isotropic laminate leads to a decrease in tensile [5] and compressive [6] strengths. For the LVI loading, Fuoss et al. [7] reported that the clustering of plies weakens the resistance of laminates to impact damage, resulting in larger delamination areas, but their work was quasi-static loading. In a study conducted by González et al. [8], impact experiments were performed, revealing that enhanced ply clustering reduces the resistance of composites against LVI damage by lowering the delamination threshold and peak loads.

Detecting the underlying mechanisms of such damages in composites during the low-velocity impact (LVI) events poses a significant challenge in both experimental and numerical investigations. While utilizing beam specimens allows for macroscopic in-situ observations, the rapid nature of impact events complicates the process of investigating damage mechanisms. To tackle this challenge, numerous researchers have focused on quasi-static indentation (QSI) experiments to qualitatively identify the damage mechanisms that take place during LVI events [9–13] because the overall impact response and failure modes has been demonstrated to show strong correlation with the quasi-static test setup. Moreover, Bozkurt and Coker [14] has revealed that the similarities between LVI and QSI experiments extend beyond just the global response to encompass dynamic aspects like delamination propagation speeds.

In this study, we conducted LVI and QSI experiments on CFRP beam specimens with two distinct cross-ply layup configurations: $[0_4/90_4/0_2]$s and $[0_2/90_2/0_2/90_2/0_2]$s. Despite both configurations having an equal number of 0° and 90° plies, they differ in terms of how these plies are clustered within the laminate. This difference allowed us to explore the influence of ply clustering on the mechanisms of LVI-induced damage. Our motivation for conducting QSI experiments was to qualitatively identify the micro-scale damage mechanisms observed during LVI events, using magnified in-situ observations facilitated by a traveling digital microscope. Then, we carried out numerical simulations of the LVI experiments using the finite element method in ABAQUS/Explicit platform. To account for fiber breakage and matrix cracking, we employed a three-dimensional continuum damage mechanics approach that incorporates the maximum stress and LaRC05 damage initiation criteria, with a linear softening damage progression. The comparison between numerical simulations and experimental observations allowed us to elucidate further the damage mechanisms seen in cross-ply laminates.

2 EXPERIMENTAL WORK

We performed low-velocity impact (LVI) and quasi-static indentation (QSI) tests on CFRP composite beams with two different layups: $[0_4/90_4/0_2]$s and $[0_2/90_2/0_2/90_2/0_2]$s. The LVI experiments utilized a non-standard drop-weight setup built by Bozkurt and Coker [14]. We provide a general description of the setup in this study; however, detailed information is available in the corresponding reference.

QSI experiments were conducted to qualitatively identify the damage mechanisms observed during LVI loading. The QSI experiments used the same impactor (referred to as the indenter in QSI experiments) and boundary configuration as the LVI experiments, with the only difference being that the loading was applied quasi-statically using an electromechanical testing machine. The subsequent sections provide details on the materials and specimen configurations, experimental setups with employed instruments, and experimental procedures.

2.1 Materials and specimen configurations

The composite specimens were fabricated using Hexcel HexPly 913/HTA unidirectional prepreg carbon fibers and epoxy through hand-layup technique. Beam specimens were obtained by cutting the manufactured plates with a water jet, resulting in in-plane dimensions of 17 mm×150 mm. The thickness of all specimens was approximately 2.5 mm.

To prepare specimens for the LVI tests, one side of the composite beams was polished using SiC grinding papers on a polishing machine. Both sides of the composite beams were polished for the QSI tests using the same procedure. Prior to conducting the tests, the polished surfaces of the beams were examined using a digital microscope to ensure there were no visible voids or manufacturing defects. Microscope photographs depicting the layup sequences of the untested $[0_4/90_4/0_2]$s and $[0_2/90_2/0_2/90_2/0_2]$s specimens are presented in Figure 1.

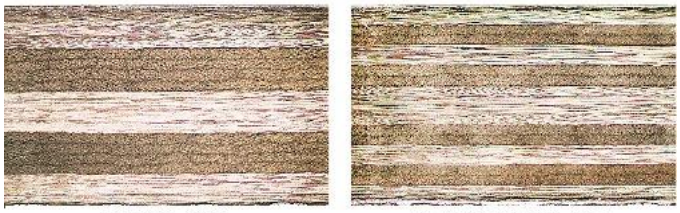

Figure 1: Layup sequences of untested specimens.

2.2 Experiment setups

The non-standard drop-weight LVI and QSI experiment setups are described in this section. Figure 2 depicts the utilized specimen and boundary configuration, and the setups for both LVI and QSI experiments.

Figure 2(a) presents the specimen, impactor/indenter, and clamped boundary configuration employed in both LVI and QSI experiments. A semi-cylindrical impactor/indenter made of steel, with a radius of 20 mm, was used to uniformly load the specimens in a two-dimensional arrangement. This line-loading approach enabled the observation of failure mechanisms from the visible edge of the specimens. The composite specimens were positioned beneath the impactor/indenter, making contact with the center of the beam specimens. Steel plates clamped the specimens from both ends. The unsupported span length between the steel plates was set at 50 mm. Figure 2(b) shows the LVI experiment setup, including the ultra-high-speed camera and light systems. The Photron SA5 ultra-high-speed camera monitored the visible edge of the specimen during impact events. The total weight of the drop-weight assembly sliding down on steel guiding shafts with the impactor was 1865 grams. Figure 2(c) presents the QSI experiment setup. It employed the same clamped boundary configuration and impactor/indenter as the LVI experiments, as shown in Figure 2(a). However, in the QSI experiments, loading was applied quasi-statically using the Shimadzu AGS-J electromechanical testing machine. During the experiments, the visible edges of the specimen were monitored using a high-resolution Canon EOS-1D digital camera on the front side and a Huvitz HDS-2520Z traveling microscope on the rear side.

2.3 Procedures

Four experiments, one low-velocity impact (LVI) test and one quasi-static indentation (QSI) test for each of the $[0_4/90_4/0_2]$s and $[0_2/90_2/0_2/90_2/0_2]$s layups, were carried out.

(A) Specimen and BCs configuration:

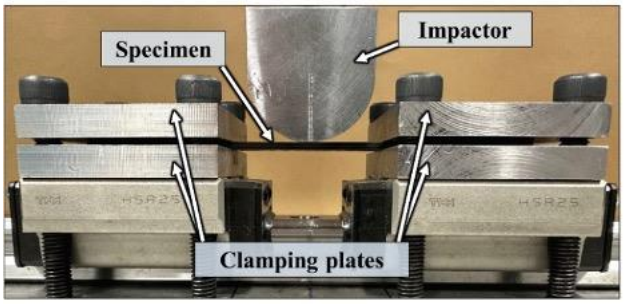

(B) LVI setup:

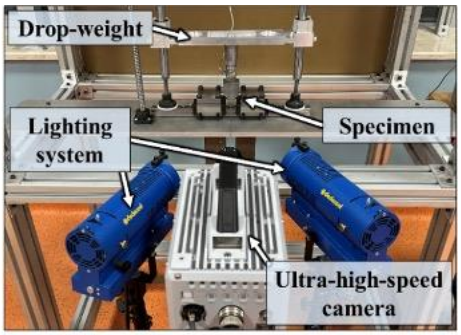

(C) QSI setup:

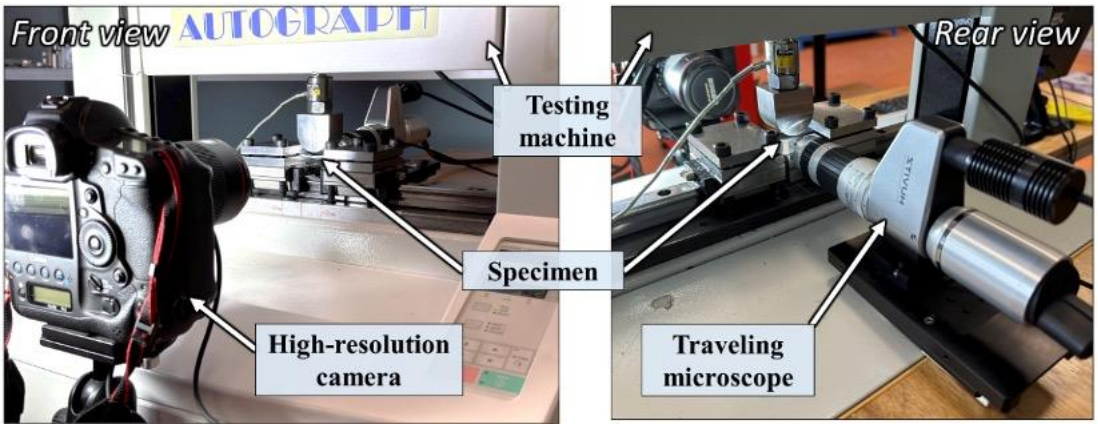

Figure 2: **(A)** Specimen, impactor/indenter and clamped boundary conditions configuration in both low-velocity impact (LVI) and quasi-static indentation (QSI) experiments, **(B)** LVI setup including ultra-high-speed camera and lighting systems, **(C)** Front view (left) and rear view (right) of the QSI setup, including a high-resolution digital camera and a traveling microscope.

During the LVI experiments, the formation and propagation of damage were monitored from the polished visible edge of the specimen using an ultra-high-speed camera system. The LVI experiments were recorded at 25,000 frames per second (fps), resulting in an interframe time of 0.04 milliseconds between each photograph.

The QSI experiments were conducted using the Shimadzu AGS-J electromechanical testing machine, with loading applied quasi-statically under displacement control at a crosshead speed of 0.5 mm/min. During the QSI experiments, the polished visible edge of the specimen was monitored using a traveling microscope with a resolution of 1600×1200 pixels. For the $[0_2/90_2/0_2/90_2/0_2]$s and $[0_4/90_4/0_2]$s specimens, microscope magnifications of 25× and 50× were used, respectively, to capture regions of 15.3 mm×11.5 mm and 7.4 mm×5.6 mm.

2.4 Experimental results

Figure 3(A) and Figure 3(B) show the damage progression of the impact-induced matrix cracking and delamination damage in $[0_4/90_4/0_2]$s and $[0_2/90_2/0_2/90_2/0_2]$s specimens, respectively. These images, captured using a high-speed camera, depict three frames from the moment of initial contact to the observation of final state of the damage.

The reference frame, taken as the initial contact between the impactor and the composite specimen, is shown in Figure 3(A.1) and Figure 3(B.1), with a time of 0 ms. In the $[0_4/90_4/0_2]$s specimen, initial matrix damage is observed at 1.32 ms on the right-hand side of the beam as a

diagonal crack inside the lower 90° group of plies, inclined at approximately 53° with respect to the horizontal in Figure 3(A.3). The delamination initiated from the upper tip of the diagonal crack propagated towards the impactor, while the lower tip initiated a delamination that propagated towards the boundary region.

For the $[0_2/90_2/0_2/90_2/0_2]$s specimen, no visible damage is observed prior to 1.00 ms. However, at 1.04 ms, sudden failure occurs, including matrix cracking, fiber breakage, and delamination, within the lower 0° and 90° plies beneath the impactor, as shown in Figure 3(B.2). This matrix cracking, coupled with fiber breakage and delamination, progressively propagates to the adjacent upper plies as the impactor moves downward. Figure 3(B.3) shows this propagation of damage towards the upper regions near the second 90° layers at 1.16 ms. The specific sequence of damage modes could not be observed at this capturing rate.

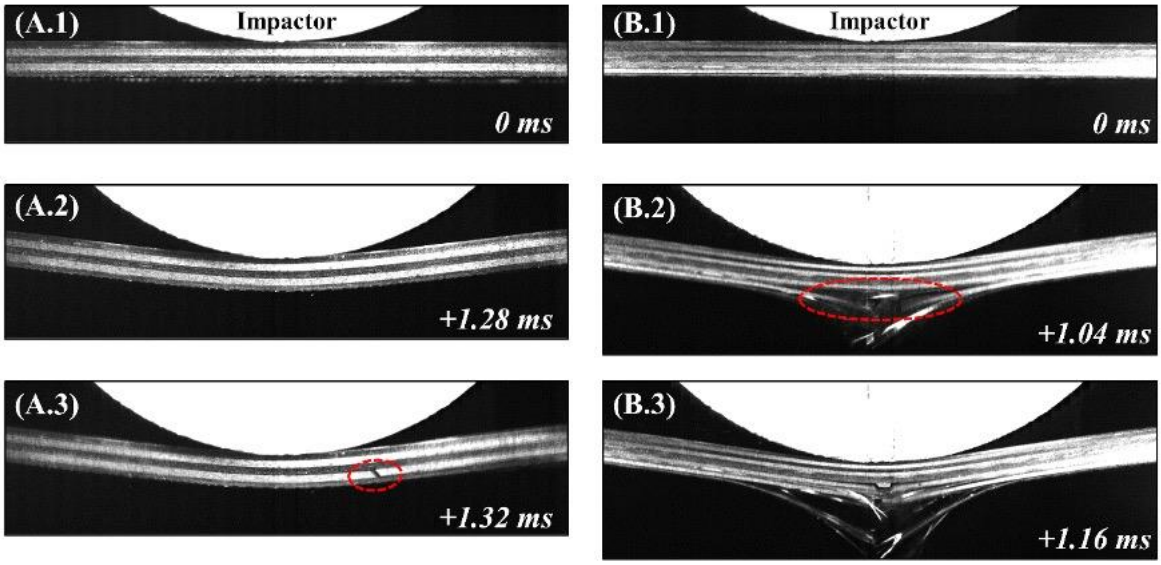

Figure 3: High-speed camera photographs showing the damage progression of **(A)** $[0_4/90_4/0_2]$s and **(B)** $[0_2/90_2/0_2/90_2/0_2]$s specimens under low-velocity impact loading.

Figure 4(A) presents the in-situ monitoring of damage progression using a traveling microscope at 25× magnification for the $[0_4/90_4/0_2]$s specimen. Figure 4(A.1) shows the early formation of a diagonal matrix crack inside the lower 90° plies. Macroscopic instruments failed to detect this crack as it was undetectable to the naked eye. Delaminations at the adjacent interfaces rapidly propagate from this matrix crack, as shown in Figure 4(A.2). Subsequently, the delamination at the upper 0°/90° interface propagates to the region beneath the indenter in Figure 4(A.3). However, this event was not captured as the matrix crack that triggered it occurred outside the microscope's field of view, only visible in Figure 4(A.3) on the left-hand side.

Figure 4(B) presents the in-situ monitoring of damage progression using a traveling microscope at 50× magnification for the $[0_2/90_2/0_2/90_2/0_2]$s specimen. Similar to the previous specimen, Figure 4(B.1) shows the initial formation of a diagonal matrix crack in the lower 90° plies preceding the delamination at the adjacent interfaces. Following this, a group of four matrix cracks on the right-hand side appeared in Figure 4(B.2). The formation of matrix crack groups is then accompanied by sudden damage growth, including fiber breakage and

delaminations, as depicted in Figure 4(B.3). We conjectured that a sudden shift in stress state led to fiber breakage in the 0° layer prior to delamination propagation.

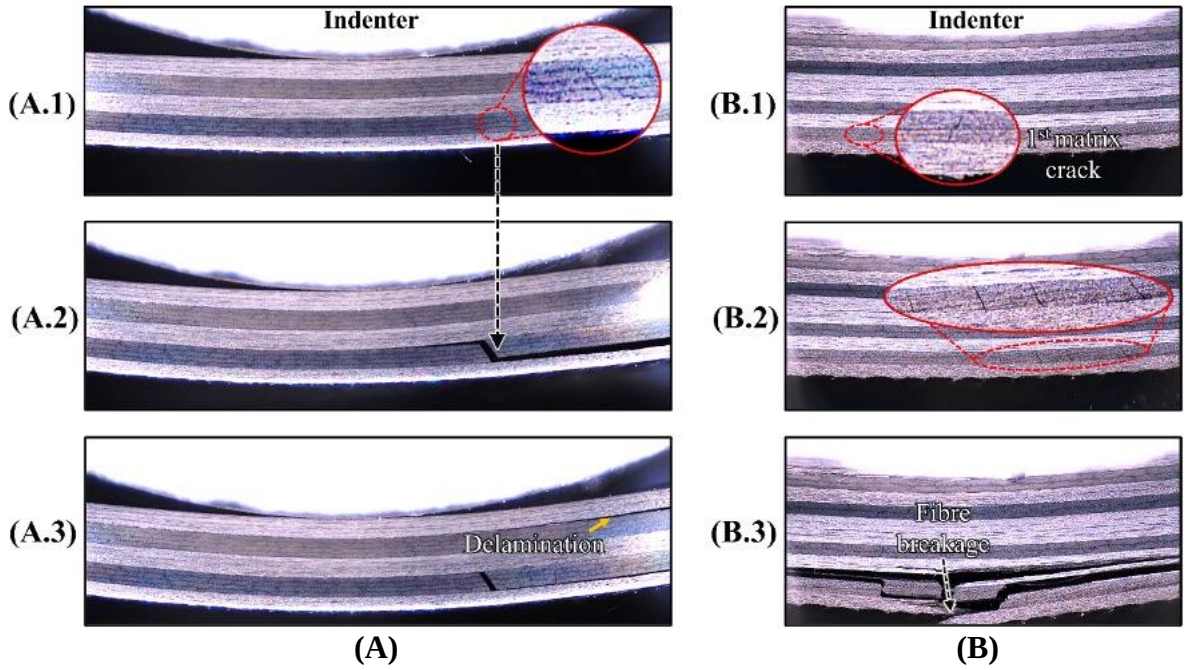

Figure 4: In-situ micrographs showing the damage progression of **(A)** $[0_4/90_4/0_2]$s and **(B)** $[0_2/90_2/0_2/90_2/0_2]$s specimens under quasi-static indentation loading.

3 NUMERICAL WORK

Numerical simulations of the low-velocity line impact experiments presented in Section 2 are constructed in the commercially available FE package ABAQUS/Explicit [15]. The specifics of the numerical models are described in the following subsections.

3.1 Intralaminar damage model

The orthotropic constitutive material model used to predict composite damage is implemented using a VUMAT subroutine in ABAQUS/Explicit. For fiber breakage and matrix cracking, a three-dimensional Continuum Damage Mechanics (CDM) approach incorporating the maximum stress and LaRC05 [16] damage initiation criteria along with a linear softening damage progression is employed. This implementation takes into account the three-dimensional stress states and in situ effects.

In the intralaminar damage model, the relationship between the bilinear equivalent stress (σ_{eq}) and equivalent displacement (δ_{eq}) that an integration point follow is illustrated in Figure 5. The material exhibits linear behavior until reaching the point of damage initiation (marked as A), which is determined by the damage initiation criteria. Equation (1) is used to predict fiber damage, while Equation (2) is employed for matrix damage, both equations predict the point of damage initiation when their value reaches unity.

$$\mathrm{FI}_{\mathrm{fiber}} = \frac{\sigma_{11}}{\mathrm{X_T}} \tag{1}$$

$$\mathrm{FI}_{\mathrm{matrix}} = \left(\frac{\tau_{\mathrm{T}}}{\mathrm{S_T} - \eta_{\mathrm{T}}\sigma_{\mathrm{N}}}\right)^2 + \left(\frac{\tau_{\mathrm{L}}}{\mathrm{S_L} - \eta_{\mathrm{L}}\sigma_{\mathrm{N}}}\right)^2 + \left(\frac{\langle\sigma_{\mathrm{N}}\rangle_+}{\mathrm{Y_T}}\right)^2 \tag{2}$$

where the traction components on the fracture plane (τ_T, τ_L, σ_N) are obtained by stress transformation relations given in Eqns. (3), (4) and (5).

$$\tau_T = -\frac{\sigma_2 - \sigma_3}{2}\sin(2\alpha) + \tau_{23}\cos(2\alpha) \tag{3}$$

$$\tau_L = \tau_{12}\cos(\alpha) + \tau_{31}\sin(\alpha) \tag{4}$$

$$\sigma_N = \frac{\sigma_2 + \sigma_3}{2} + \frac{\sigma_2 - \sigma_3}{2}\cos(2\alpha) + \tau_{23}\sin(2\alpha) \tag{5}$$

Once the damage initiation criterion is met, the material undergoes progressive damage by reducing the stiffness of the elements, which is achieved by introducing damage multipliers into the compliance tensor. Figure 5 shows the linear softening response of the damage evolution where the area under the curve is characterized by the energy dissipated until complete failure G_c. Depending on the failure mode, it is taken to be the same as the fracture toughness associated with fiber (G_{1+} = 81.5 kJ/m^2) and transverse tensile (G_{2+} = 0.26 kJ/m^2) failure modes.

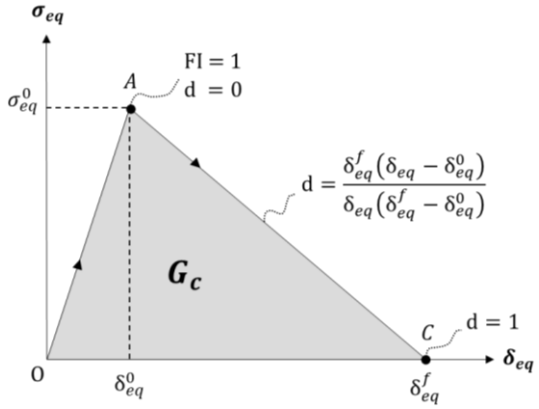

Figure 5: Constitutive material model that predicts the intralaminar damage initiation and progression.

3.2 Finite element model

Figure 6 illustrates the geometry and boundary conditions of the FE model employed in the analyses. The semi-cylindrical steel impactor is represented as a rigid body with a mass of 1.865 kg. It is positioned just above the mid-span of the composite beam. To simulate the free fall of the impactor, an initial downward velocity of 3.57 m/s is assigned to the impactor. The composite beam specimen is modeled as a three-dimensional deformable body. The boundary conditions are defined at the end regions of the beam, in accordance with the experiments, with dimensions of 50×17 mm^2. The bottom surface regions are fixed in both the longitudinal and transverse directions, while the top surfaces are fixed only in the longitudinal direction to account for specimen contraction due to Poisson's ratio effect.

For in-plane element sizing, the greatest in-plane size $l^* = \sqrt{l_x l_y}$ is suggested to be less than the maximum in-plane characteristic length $2E_M G_M / X_M{}^2$ to avoid the snap-back behavior [17], where E_M, G_M and X_M are elastic modulus, fracture toughness and strength values. The values of M correspond to different failure modes: M=1$^+$ and M=1$^-$ for fiber tensile and compressive, M=2$^+$ and M=2$^-$ for matrix tensile and compressive, and M=6 for shear damage. Along the thickness direction, mesoscale modeling is implemented for the composite elements, with each ply represented by a single layer of solid elements. As a result, the mesh sizes for the in-plane and along the thickness directions are determined as 0.2×0.2 mm^2 and 0.125 mm, respectively.

The composite elements employed in the FE model are 8-noded linear brick elements with reduced integration and enhanced hourglass control (referred to as C3D8R in the ABAQUS library). To account for large deflections that result in changes in stiffness, the nonlinear geometry option is activated.

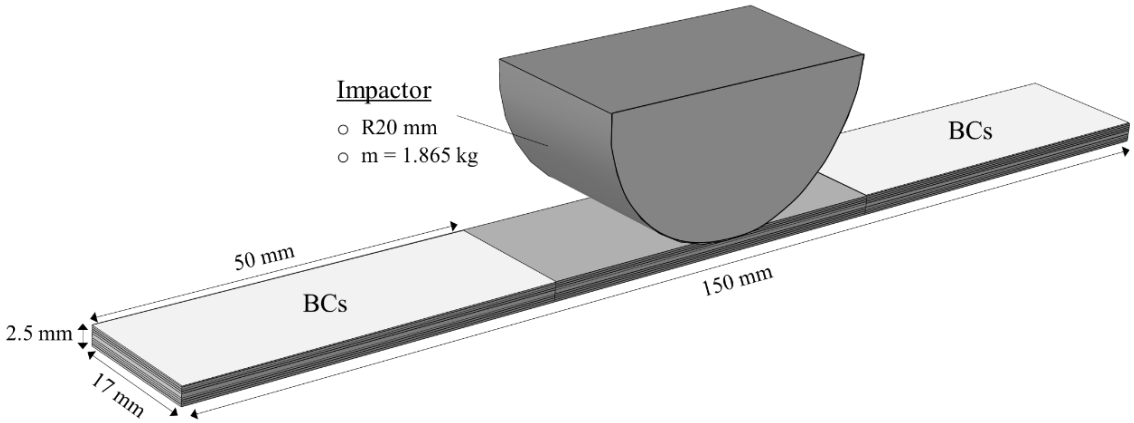

Figure 6: Geometry and boundary conditions of the numerical impact test setup.

The material properties of the Hexcel 913C/HTS unidirectional (UD) prepreg utilized in the simulations can be found in Table 2.

Table 1 Material properties used in simulations.

Elastic properties	E_1 = 135 GPa; $E_2 = E_3$ = 9.2 GPa;
	$G_{12} = G_{13}$ = 5.5 GPa; G_{23} = 4.5 GPa;
	$\nu_{12} = \nu_{13}$ = 0.30; ν_{23} = 0.45
Ply-level strength	X_T = 2200 MPa; X_C = 1500 MPa
	$Y_T = Z_T$ = 60 MPa; $Y_C = Z_C$ = 205 MPa; S_L = 62 MPa
Density	ρ = 1780 kg/m^3

Contact and friction laws are defined between the steel impactor and composite beam, and between composite layers in case self-contact. Different coefficients of friction (COFs) are employed depending on the contact couples: a COF of 0.3 for the contact between the steel impactor and the composite, and a COF of 0.5 in case of self-contact between the composite layers.

3.3 Numerical results

Figure 7 depicts the distributions of full-field longitudinal (ε_{xx}) and transverse shear (γ_{xy}) strains, and the matrix failure index across the $[0_4/90_4/0_2]$s specimen prior to damage. In Figure 7(A), areas with elevated ε_{xx} values are concentrated just beneath the impactor and in the upper regions adjacent to the boundaries. Meanwhile, γ_{xy} field in Figure 7(B) exhibit elevated values near boundaries and within a cone-shaped region beneath the impactor inside the 90° plies. The matrix failure index values reaching unity beneath the impactor and near the boundaries within the lower and upper 90° ply groups, respectively. Simultaneously comparing Figure 7(A), (B) and (C) indicates that the failure initiates due to a shear-dominated stress state, as higher failure index values align with regions of elevated γ_{xy}.

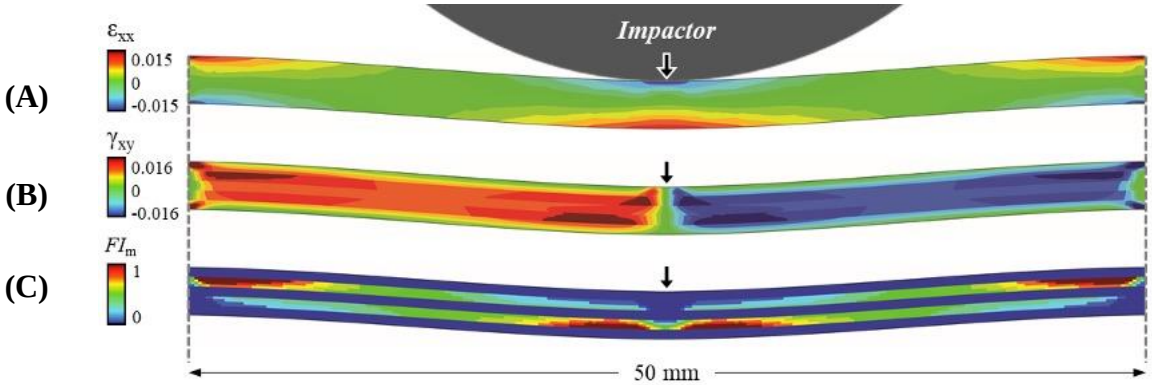

Figure 7: **(A)** Longitudinal strain (ε_{xx}) and **(B)** transverse shear strain (γ_{xy}) fields, and **(C)** distribution of matrix failure index along the $[0_4/90_4/0_2]$s specimen prior to damage.

Figure 8 depicts the full-field ε_{xx} and γ_{xy} strain fields, and the distribution of fiber and matrix failure indices across the $[0_2/90_2/0_2/90_2/0_2]$s specimen prior to damage. Similar to the preceding layup, Figure 8(A) displays areas of elevated ε_{xx} values concentrated just beneath the impactor and in upper regions adjacent to the boundaries. γ_{xy} field in Figure 8(B) exhibit elevated values near boundaries and within a cone-shaped region beneath the impactor inside the 90° plies. Fiber and matrix failure index values reaching unity are observed beneath the impactor within the lower group of 0° plies and the upper group of 90° plies, respectively. A simultaneous examination of Figure 8(A), (B), (C) and (D) indicates that failure initiates due to a tensile-dominated stress state, as higher failure index values align with regions of increased ε_{xx}.

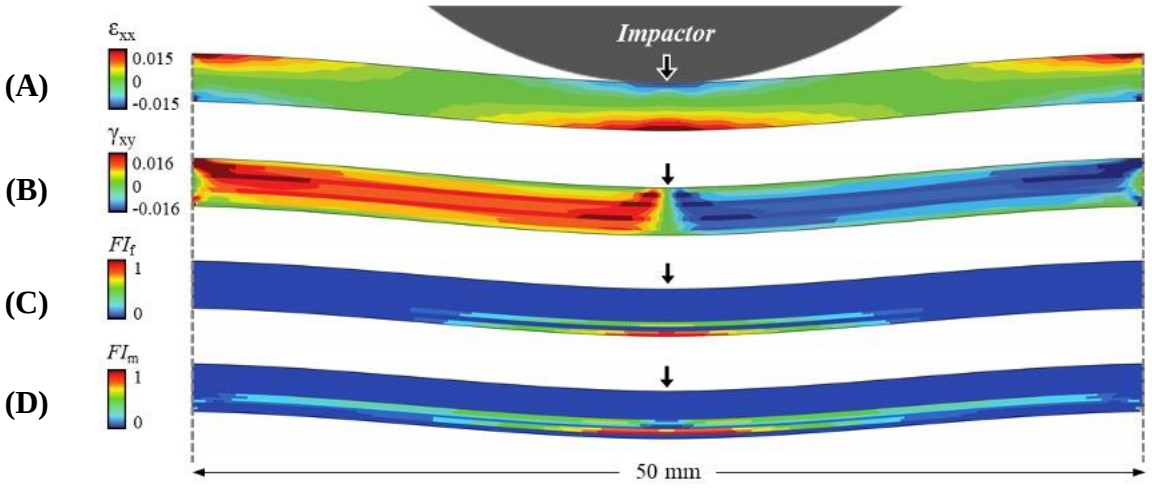

Figure 8: **(A)** Longitudinal strain (ε_{xx}) and **(B)** transverse shear strain (γ_{xy}) fields, and **(C)** distribution of failure indices along the $[0_2/90_2/0_2/90_2/0_2]$s specimen prior to damage.

Predictions for the matrix fracture angle orientations in the $[0_4/90_4/0_2]$s and $[0_2/90_2/0_2/90_2/0_2]$s specimens prior to damage initiation are presented in Figure 9. These angles are calculated by searching for the angle that maximizes the matrix failure index given in Equation (2). Both specimens exhibit similar distributions for the fracture angle predictions, where angles respectively become vertical and horizontal in the lower and upper 90° plies from boundaries to center of the beam. Notably, the $[0_2/90_2/0_2/90_2/0_2]$s specimen exhibits a more noticeable variation in predictions along the horizontal direction compared to $[0_4/90_4/0_2]$s specimen.

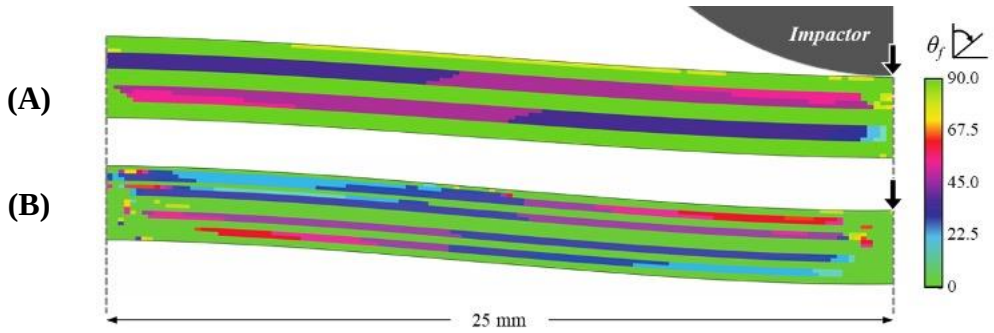

Figure 9: Predictions for the matrix fracture angle orientations prior to damage initiation of **(A)** $[0_4/90_4/0_2]$s and **(B)** $[0_2/90_2/0_2/90_2/0_2]$s specimens.

Development of the damage in the $[0_4/90_4/0_2]$s specimen is presented in Figure 10. The first frame at 420 μs shows that the onset of damage underneath the impactor and near the boundaries at the 0°/90° interfaces, in line with the damage initiation predictions in Figure 7(C). Damage vertically grows in a periodic manner within these regions, as it can be seen in the frames at 460 μs and 474 μs. By 476 μs, a damage, in the form of delamination along the adjacent elements of the upper 0° plies, propagated towards the impactor within the upper 90° plies unlike the case seen in the experiments where damage initiated at the lower 90° ply group. The reason for such difference is attributed to the effect of the fixed boundary conditions in the modeling, which is believed to introduce virtual inaccuracies compared to the experimental boundaries. Damages originating from opposite sides of the beam merge at the center by 478 μs.

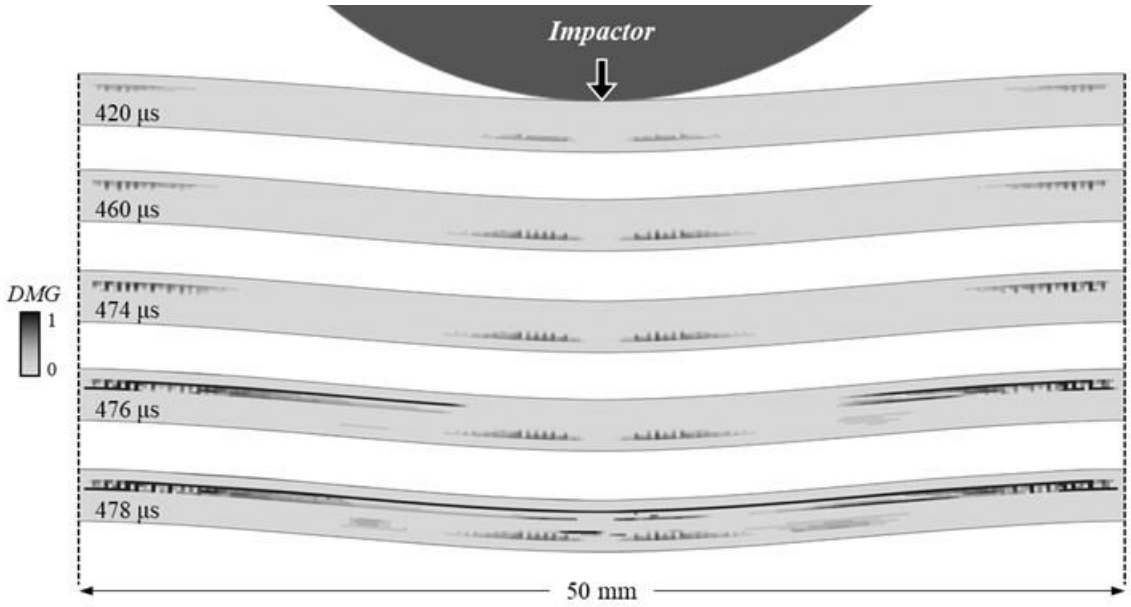

Figure 10: Development of the damage in the $[0_4/90_4/0_2]$s specimen.

Development of the damage in the $[0_2/90_2/0_2/90_2/0_2]$s specimen is presented in Figure 11. The first frame at 580.5 μs reveals the presence of vertical matrix cracking beneath the impactor, occurring specifically within the lower 90° plies underneath it. By 518 μs, a damage, in the form of delamination along the adjacent elements of the lower 0° plies, propagated towards the boundaries within the lower 90° plies. At 519.5 μs, elements located at the center

of the lower 0° ply group are deleted due to complete fiber damage. As the delamination-like damage propagates to the boundaries, a subsequent vertical matrix crack becomes evident within the adjacent upper 90° plies at 532.5 μs. Similarly, this matrix crack triggers a sequence of events of delamination-like damage at 534 μs and fiber breakage at 535 μs The observed damage patterns correspond well with the experimental outcomes presented in Figure 3(B), with the FE simulation revealing a sequence beginning with matrix cracking followed by fiber damage.

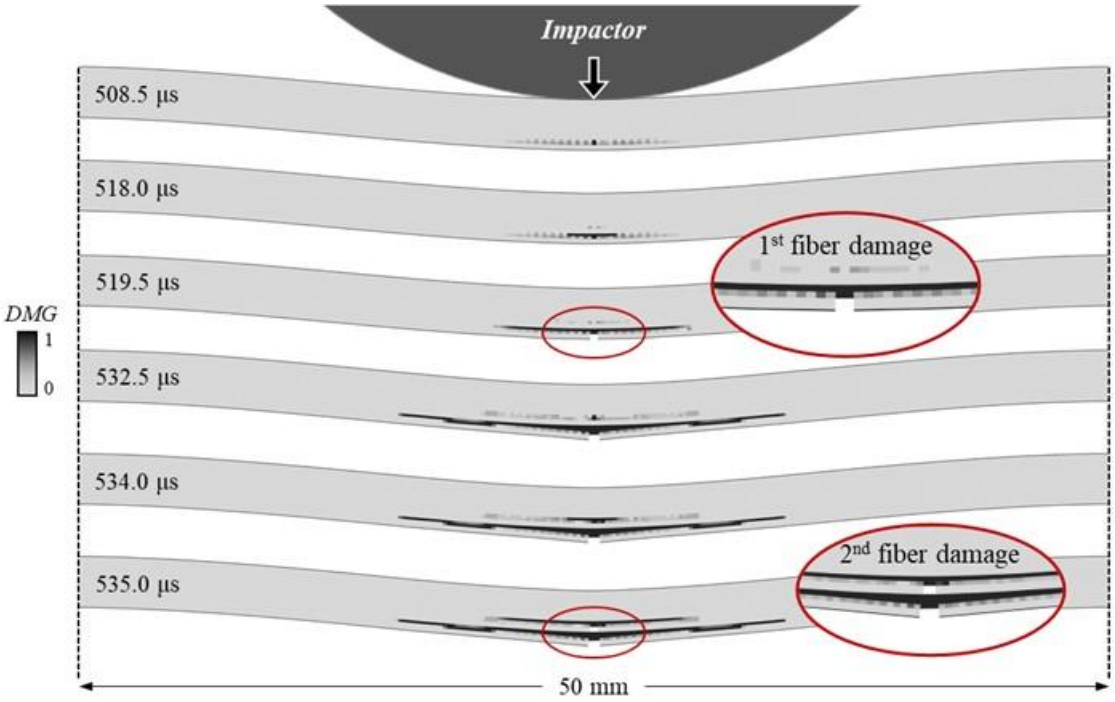

Figure 11: Development of the damage in the $[0_2/90_2/0_2/90_2/0_2]$s specimen.

4 CONCLUSIONS

In this study, we performed in-situ low-velocity impact (LVI) and quasi-static indentation (QSI) experiments on CFRP composite beams with two different layup configurations ($[0_4/90_4/0_2]$s and $[0_2/90_2/0_2/90_2/0_2]$s). First, we observed that the experiment results on specimens with identical layup configurations displayed remarkable consistency between LVI and QSI experiments in terms of damage patterns. Second, our experimental findings indicate that clustering a smaller number of 90° plies ($[0_2/90_2/0_2/90_2/0_2]$s specimen) leads to a damage mechanism that involves matrix cracking, delamination, and fiber breakage. Conversely, the clustering of a greater number of 90° plies ($[0_4/90_4/0_2]$s specimen) results in the demonstration of matrix cracking and delamination damages exclusively, without any apparent fiber breakage. Following the experiments, we performed numerical simulations of the LVI experiments. The simulation results are in good agreement in terms of damage patterns and sequences with the experiments. However, it's worth noting that the initial damage location in the $[0_4/90_4/0_2]$s model differed from experimental observations, which is attributed to the virtual effect of the fixed boundary conditions modeling. The simulation results for the $[0_2/90_2/0_2/90_2/0_2]$s configuration revealed the damage sequence of delamination followed by fiber breakage, which could not captured explicitly in the corresponding experiments.

REFERENCES

[1] Abrate S. Impact on Composite Structures. Cambridge: Cambridge University Press; 1998. https://doi.org/10.1017/CBO9780511574504.

[2] Parvizi A, Garrett KW, Bailey JE. Constrained cracking in glass fibre-reinforced epoxy cross-ply laminates. J Mater Sci 1978;13:195–201. https://doi.org/10.1007/BF00739291.

[3] Flaggs DL, Kural MH. Experimental Determination of the In Situ Transverse Lamina Strength in Graphite/Epoxy Laminates. Journal of Composite Materials 1982;16:103–16. https://doi.org/10.1177/002199838201600203.

[4] Camanho PP, Dávila CG, Pinho ST, Iannucci L, Robinson P. Prediction of in situ strengths and matrix cracking in composites under transverse tension and in-plane shear. Composites Part A: Applied Science and Manufacturing 2006;37:165–76. https://doi.org/10.1016/j.compositesa.2005.04.023.

[5] Wisnom MR, Khan B, Hallett SR. Size effects in unnotched tensile strength of unidirectional and quasi-isotropic carbon/epoxy composites. Composite Structures 2008;84:21–8. https://doi.org/10.1016/j.compstruct.2007.06.002.

[6] Wisnom MR, Hallett SR, Soutis C. Scaling Effects in Notched Composites. Journal of Composite Materials 2010;44:195–210. https://doi.org/10.1177/0021998309339865.

[7] Fuoss E, Straznicky PV, Poon C. Effects of stacking sequence on the impact resistance in composite laminates — Part 1: parametric study. Composite Structures 1998;41:67–77. https://doi.org/10.1016/S0263-8223(98)00036-1.

[8] González EV, Maimí P, Camanho PP, Lopes CS, Blanco N. Effects of ply clustering in laminated composite plates under low-velocity impact loading. Composites Science and Technology 2011;71:805–17. https://doi.org/10.1016/j.compscitech.2010.12.018.

[9] Kaczmarek H, Maison S. Comparative ultrasonic analysis of damage in CFRP under static indentation and low-velocity impact. Composites Science and Technology 1994;51:11–26. https://doi.org/10.1016/0266-3538(94)90152-X.

[10] Bull DJ, Spearing SM, Sinclair I. Investigation of the response to low velocity impact and quasi-static indentation loading of particle-toughened carbon-fibre composite materials. Composites Part A: Applied Science and Manufacturing 2015;74:38–46. https://doi.org/10.1016/j.compositesa.2015.03.016.

[11] Weirdie BL, Lagace PA. On the Use of Quasi-Static Testing to Assess Impact Damage Resistance of Composite Shell Structures. Mechanics of Composite Materials and Structures 1998;5:103–19. https://doi.org/10.1080/10759419808945895.

[12] Wagih A, Maimí P, González EV, Blanco N, de Aja JRS, de la Escalera FM, et al. Damage sequence in thin-ply composite laminates under out-of-plane loading. Composites Part A: Applied Science and Manufacturing 2016;87:66–77. https://doi.org/10.1016/j.compositesa.2016.04.010.

[13] Abisset E, Daghia F, Sun XC, Wisnom MR, Hallett SR. Interaction of inter- and intralaminar damage in scaled quasi-static indentation tests: Part 1 – Experiments. Composite Structures 2016;136:712–26. https://doi.org/10.1016/j.compstruct.2015.09.061.

[14] Bozkurt MO, Coker D. In-situ investigation of dynamic failure in [05/903]s CFRP beams under quasi-static and low-velocity impact loadings. International Journal of Solids and Structures 2021;217–218:134–54. https://doi.org/10.1016/j.ijsolstr.2021.01.032.

[15] Hibbitt H, Karlsson B, Sorensen P. Abaqus analysis user's manual version 6.10 2016.

[16] Pinho S, Darvizeh R, Robinson P, Schuecker C, Camanho P. Material and structural response of polymer-matrix fibre-reinforced composites. Journal of Composite Materials 2012;46:2313–41. https://doi.org/10.1177/0021998312454478.

[17] González EV, Maimí P, Camanho PP, Turon A, Mayugo JA. Simulation of drop-weight impact and compression after impact tests on composite laminates. Composite Structures 2012;94:3364–78. https://doi.org/10.1016/j.compstruct.2012.05.015.